Mechanical white etching layer formation kinetics in pearlitic steels: A phenomenological model based on microstructural characterization

Léo Thiercelin [a,*], Sophie Cazottes [b], Pierrick Merino [c], Aurélien Saulot [c], Frédéric Lebon [d]

[a] *Arts et Métiers Institute of Technology, CNRS, Université de Lorraine, LEM3-UMR 7239, F-57078 Metz, France*
[b] *Université de Lyon, INSA Lyon, CNRS UMR 5510, MATEIS, F-69621, Villeurbanne, France*
[c] *Université de Lyon, INSA Lyon, CNRS UMR 5259 LaMCoS, F-69621, Villeurbanne, France*
[d] *Aix Marseille Université, CNRS, Centrale Marseille, LMA UMR 7031, F-13453 Marseille, France*

ABSTRACT

In order to predict the lifetime of railtrack components, numerical models are required to better describe the apparition of microstructural defects that lead to material failure. In pearlitic steels, the severe mechanical loading or/and the local temperature increase result in the formation of a hard and brittle phase that is prone to cracking, which is called White Etching Layer (WEL).

The current study proposes a phenomenological model, based on the microstructural evolution, to describe the mechanically-induced-WEL kinetics of formation. First, a detailed multiscale microstructural characterization was performed in order to identify suitable microstructural indicators for the WEL formation. The grain size, orientation and morphology, and internal disorientation were characterized for different steps of mechanical WEL formation. This could be achieved thanks to the use of a dedicated test bench that allows to monitor the wheel–rail contact condition (sliding, number of cycles, and contact pressure) independently. The proposed model was validated using tests performed in extreme load and sliding conditions.

The numerical and experimental results indicate that the most severe conditions (contact pressure and sliding ratio) catalyze WEL formation, and that the same deformation state can be achieved through different loading paths.

1. Introduction

The severe loading induced on the steel rails can produce different types of rolling-contact fatigue (RCF) defects that can result in rail failure. Several damage mechanisms, including cyclic plasticity and tribological surface transformation (TST), are responsible for this defect formation. The main defects encountered are squats [1] and head checks [2]. From a metallurgical perspective, these defects are often the consequence of crack initiation induced by material microstructural changes. The first type of evolution is severe plastic deformation of the surface, which can either modify the profile of the rails (corrugation) or induce fibering of the microstructure that then leads to cracks. The second type of evolution concerns the formation of TST, which leads to cracks at the interfaces because of the incompatibility between the initial phase and the TST or within the TST itself [3]. Two types of TST are observed on rail surfaces: the formation of a white etching layer (WEL) or a brown etching layer [3–5]. WEL formation affects all grades of rail steels in almost all railway networks (France [1,6,7] United Kingdom [8,9], Germany [10–12], the Netherlands [3,5], Australia [13,14] or Japan [15]).

The formation of WELs leads to the transformation of pearlitic steel with grains with sizes of some dozen of micrometers into a nanocrystalline and brittle structure [16,17]. The final WEL structure depends on the loading history of the rail but is generally a mixture of various phases such as residual austenite [18], fragmented cementite [3,5,18], martensite [12,13,19] and ferrite supersaturated in carbon [9, 16,20] following fragmentation of the grains and a redistribution of the carbon atoms.

Because of the different structures of WELs, the authors have proposed two extreme scenarios of WEL formation. The first type are thermal WELs with a martensitic structure and the presence of residual austenite [12,13,19]. Such WELs result from a temperature increase above the austenitization temperature (720 °C) followed by rapid cooling. These temperature rises are associated with significant wheel slippage in relation to the rail [16,21] or the formation of adiabatic shear bands [22].

Under other conditions where the temperature does not exceed a few hundred degrees, the severe multiaxial stresses and the

accumulation of plastic deformation lead to a progressive evolution of the microstructure, ultimately resulting in WEL formation [9,10,16,21,23,24]. Thus, the WEL formation is associated with a complex thermomechanical coupling whose loading history is not unique [25].

In this paper, we will focus on the mechanisms of the WEL formation steps induced mainly mechanically for pearlitic rail steels. To produce a highly fragmented and dislocated microstructure, the microstructure undergoes a succession of transformations that can be roughly divided into several characteristic stages: fibering of the grains and reduction of the interlamellar spacing [8,26–30], nanostructuring of grains [23,31–36], dissolution of the cementite, and finally redistribution of the carbon atoms [3,18,37,38].

The complexity of the mechanisms of the mechanical WEL formation makes modeling difficult as several scales are required to capture all the processes. The existing models of WEL formation are mainly based on a thermal mechanism with significant temperature increases beyond the austenitization temperature [39–41]. Antoni et al. [42] proposed the first macroscopic model to predict WEL formation by introducing a thermomechanical coupling that considers the effect of hydrostatic pressure on the austenitization temperature. The model describes the behavior of the material volume in response to a thermomechanical stress. In this model, an internal variable is considered to reflect the transition from the initial pearlitic state to the final WEL state. However, this model has presented some limitations on the thermomechanical coupling introduced (the pressure–temperature coupling is insufficient) and on the interpretation of the internal variable, which is defined as a fraction of fully transformed phase without considering the transient stages. Thiercelin et al. [43] enhanced this initial model by adding the dependence on shear stress. Moreover, the internal metallurgical variable was also reinterpreted to consider the different stages of microstructural evolution by characterizing the microstructural gradient of highly deformed rails with or without WELs.

The aim of the current work was to determine the microstructural indicators that reflect the progressive formation of WELs and to link them to internal variables of the model proposed in [43]. To provide a model that could be widely and industrially used, indicators were selected that can be identified using standard characterization techniques (e.g., scanning electron microscopy (SEM) with electron backscatter diffraction (EBSD), optical microscopy, hardness testing). First, several microstructures characteristic of the different stages of transformation were analyzed. These microstructures were obtained from representative tests of wheel–rail contact under controlled thermomechanical conditions [33,34] and from a WEL sample extracted from a squat zone [1]. Then, a set of several microstructural parameters were proposed to describe the different stages of transformation leading to the final stage of WEL formation. These parameters enabled correlation of the EBSD data with the internal variables of the model of WEL formation [43]. A phenomenological model of mechanically-induced white etching layer formation based on microstructural characterization was proposed. Finally, the approach was applied to "validation tests" that are part of the continuation of the work of Merino [33] and Lafilé [34] under more severe conditions (slip, contact pressure). The effects of these extreme contact conditions on the WEL formation kinetics are discussed numerically and experimentally. The expectation here was to observe microstructural evolutions approaching the final stage of WEL formation.

2. Materials and methods

2.1. Material and test bench

A cylinder-on-ring-type tribometer representative of wheel–rail contact on a 1/15 scale was previously developed to reproduce WEL formation [33,34]. It consists of a small disk of 70-mm diameter, representing the wheel rotating on a horizontal circular ring of 2-m

Table 1
Chemical composition of R260 steel (weight %) [44].

C	Si	Mn	P	S	Cr	Al
0.62	0.80	0.15 - 0.58	0.70 - 1.20	< 0.025	< 0.15	< 0.004

Table 2
Experimental conditions for the test bench; P is the Hertz contact pressure, γ is the sliding ratio (Eq (1)); and N_{cycle} is the number of the cycles performed by the ring.

Test number	Data	Test conditions	Surface treatment
#Reference	[33]	1000 cycles at $\gamma = 0\%$ and 1000 cycles at $\gamma = 0.5\%$ with a contact pressure of 1 GPa	No oxidation
#1	[33]	$P = 1$ GPa $- \gamma = 0\% - N_{cycle} = 1000$	oxidation
#2	[33]	$P = 1$ GPa $- \gamma = 0.5\% - N_{cycle} = 1000$	oxidation
#3	current study	$P = 1$ GPa $- \gamma = 1.5\% - N_{cycle} = 1000$	oxidation
#4	current study	$P = 1.3$ GPa $- \gamma = 0\% - N_{cycle} = 1000$	oxidation
#5	current study	$P = 1.3$ GPa $- \gamma = 0.5\% - N_{cycle} = 1000$	oxidation

diameter corresponding the rail (Fig. 1). Both the wheel and the ring are made of R260 pearlitic steel whose the chemical composition is given in Table 1. The material was supplied directly by SAARSTAHL Rail. This device allows control over the contact parameters expected to catalyze the kinetics of WEL formation such as contact pressure, shear induced by the sliding of the wheel on the rail, the accumulation of cycles and the wear rate. The samples from this previous testing were re-examined in relation to the work proposed in this paper. Additional experiments were performed on this test bench to confirm the initial findings. The set of test conditions used in the current study are summarized in Table 2. Control of the sliding ratio of the wheel in relation to the rail was achieved by independently monitoring the speed of rotation of the wheel and the crown. The sliding ratio, γ, can then be expressed as follows:

$$\gamma \ (\%) = \frac{V_{wheel} - V_{rail}}{\frac{1}{2}(V_{wheel} + V_{rail})} \tag{1}$$

where V_{wheel} and V_{rail} are the "linear" speed of the wheel and the rail at the point of contact, respectively.

The number of cycles refers to the number of the cycles performed by the ring. The sliding ratio was set at a realistic value ($\leq 2\%$) to initiate mechanical WEL formation [45]. For values that greatly exceed 2%, thermal WEL formation would be favored [46–48]. In addition, a specimen of R260 pearlitic steel containing WEL patches was cut from a piece of rail removed from an area of the Paris rail network prone to RCF defects (squats) [1,49].

2.2. Microstructural characterization

Optical microscopy characterization was performed after mechanical polishing down to 1 μm and subsequent Nital etching to observe cementite lamellaes and the possible WEL.

The samples were also prepared for observations in secondary electron (SE) mode and for electron backscatter diffraction (EBSD) mode in the scanning electron microscope. For the EBSD mode, the samples were mechanically polished down to 1 μm using a conventional grinding machine. The final preparation step consisted of vibratory polishing for approximately 1 h using a colloidal silica suspension (Struers OP-S) with a grain size of 0.05 μm. For some cross-section samples, it was possible to perform an additional ionic polishing step with a GATAN ILLION 2 device with an accelerating voltage of 4 kV. The observations were performed using a FEG Zeiss Supra 55VP microscope equipped
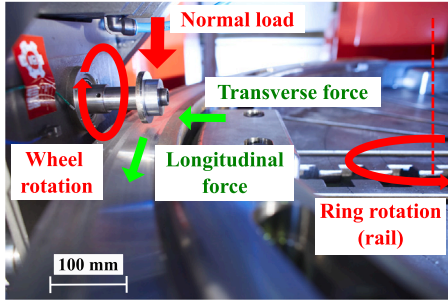
Fig. 1. Triboring test rig located at LaMCoS (INSA Lyon). The boundary conditions applied to the surface of the ring, the rotation speeds (wheel and ring) and the normal load, are indicated in red. The transverse force and the longitudinal force induced in the contact are indicated in green. (For interpretation of the references to color in this figure legend, the reader is referred to the web version of this article.)
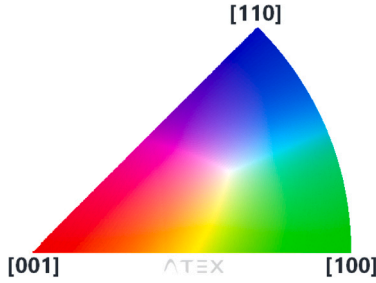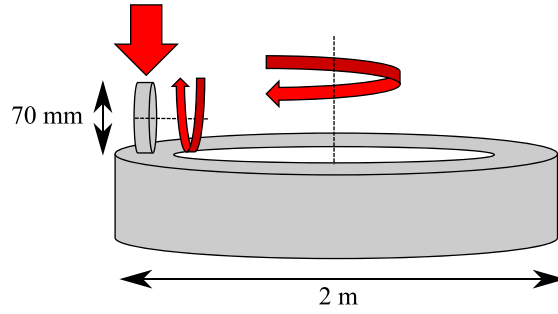

Fig. 2. Inverse pole figure color coding of orientation maps presented in this study. (For interpretation of the references to color in this figure legend, the reader is referred to the web version of this article.)

with an Oxford EBSD Symmetry detector. The accelerating voltage was set to 12 or 15 kV, depending on the size of the microstructural elements to be analyzed. The EBSD data treatment was performed using Atex software [50]. For the data treatment of the EBSD maps, the disorientation angle selected for grain detection was set to 5°, and only grains with at least 10 pixels were considered as below this level, the detection is not reliable. Fig. 2 indicates the color code used to define the crystallographic textures of all the inverse pole figures (IPF) presented in this study.

2.3. Recall of the previous model

A model of WEL formation initially developed by Antoni et al. [42] and later improved by Thiercelin et al. [43] is recalled in this section. This model is a thermodynamically based phenomenological model that introduces two types of plasticity: the plasticity classically encountered in steels and that induced by phase change ("TRansformed Induced Plasticity" known as TRIP). For the latter, an internal variable Z was introduced to quantify the state of transformation of the microstructure. This variable varies between 0 and 1, corresponding to the pearlitic steel and WEL stage, respectively. The interpretation and correlation with the indicators will be explained in the following sections. The evolution law of the internal variable was assumed to be a function of the hydrostatic pressure $P(t)$, the von Mises stress $\sigma_{eq}(t)$ and the temperature $T(t)$. It then leads to the following expression:

$$\dot{Z} = \left\langle 1 - Z \right\rangle \times g\left[P(t), \sigma_{eq}(t), T(t)\right] \tag{2}$$

where $\langle . \rangle$ denotes the Macaulay brackets ($\langle x \rangle = x$ when $x > 0$ and $\langle x \rangle = 0$ when $x \leq 0$) and $g\left[P(t), \sigma_{eq}(t), T(t)\right]$ is a function that depends on the thermomechanical stresses induced on the rail surface whose expression is given in Appendix. This function is a criterion of WEL formation that is expected to depend on three contributions: the temperature, hydrostatic pressure, and shear stress, which is captured by the von Mises equivalent stress [43]. If the thermomechanical conditions are

not satisfied for WEL formation, this function is equal to zero. In other words, the model postulates that WEL formation requires a thermomechanical coupling [3,5,10,16,25,51]. The specificity of this model is to consider that WEL formation is possible for low temperatures if the mechanical stresses are sufficient [7,9].

2.4. Scale of observations and selection of microstructural indicators

The aim of this part was to relate the Z variable defined in the previous section to the microstructural observations. It was thus necessary to identify microstructural indicators that quantitatively describe the microstructural evolution and that could be used to evaluate the value of Z for each evolution step of the WEL formation.

Microstructural observations in previous studies have revealed that a microstructural gradient is created during the wheel–rail contact to a depth of 100 μm from the contact surface [6]. However, as WELs are usually present only at the top surface, the Z variable was set to describe only the first 10 μm beneath the surface. Moreover, as microstructural evolutions are multiscale, multiple characterization techniques are needed. Indeed, the fibration of the microstructure can be observed using optical microscopy, whereas carbon redistribution requires a very local analysis, using atom probe tomography for instance [3,18,37,52].

The different stages of WEL formation have been well described to involve fibration of the microstructure, followed by a grain-size reduction, progressive dissolution of the cementite, and, finally, redistribution of the carbon (see Introduction). These microstructural evolutions could be described by the evolution of several parameters such as the hardness, grain size, grain shape, disorientation, interlamellar spacing, and carbon content. However, the hardness (or microhardness) alone was found inadequate to quantify the evolution of the transformation, as the appearance of WELs is localized to the top surface and the volume is often smaller than that usually deformed during this type of analysis (several hundreds of μm). In addition, the interlamellar spacing of pearlite would be adequate to describe only the first steps of the transformation. As soon as the fibration becomes more important, the cementite lamellas are not easily visible, and their interspacing can no longer be measured. Moreover, as the observed interlamellar spacing is directly affected by the orientation of the initial pearlite grain relative to the surface, it is not possible to quantitatively compare two different grains using this indicator alone. Finally, the measurement of the carbon concentration in ferrite is too complex to be used in an industrial context and for a large number of samples, as it requires either Mossbauer spectrometry, which is not very common [30,53], or atom probe tomography [3,18,37,52], the observations of which are very local and time consuming.

For these reasons, three microstructural indicators were selected: the grain size and the aspect ratio that is equal to 1 when the grains are spherical and tends toward $+\infty$ when the grains are very elongated. The statistical distributions of these two indicators in each EBSD
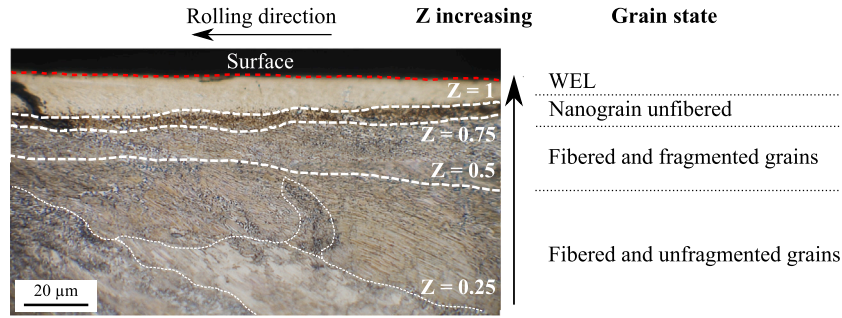
Fig. 3. Optical micrography image of longitudinal cross-section extracted from a worn rail in an area prone to developing squats [1] after Nital etching. A microstructural gradient is observed with the different stages of grain transformation from the pearlitic to WEL stage with Z associated with the different stages.
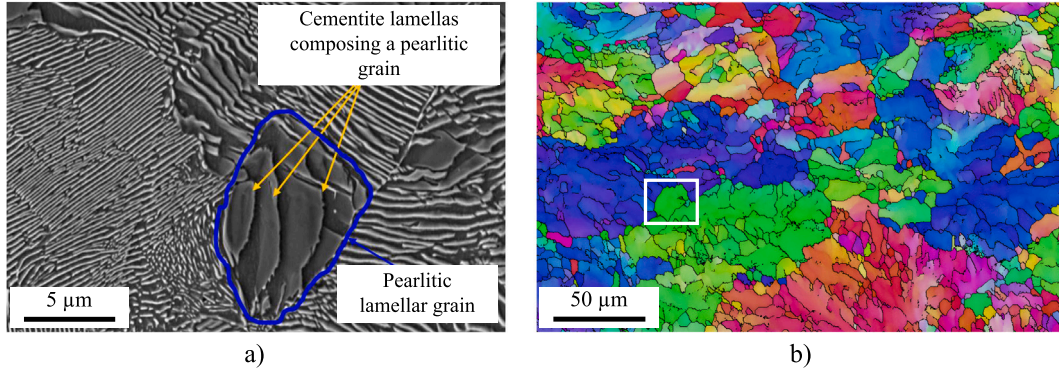

Fig. 4. Example of initial pearlitic microstructure: (a) cementite lamellas revealed by SEM-SE imaging [54] and (b) EBSD IPFZ map of the pearlitic colonies (step size = 0.3 μm). Indicators: grain size = 9.6 ± 8.1 μm; aspect ratio of 2.0 ± 0.9, grain-disorientation repartition: LAGBs = 30%, MAGBs = 41%, and HAGBs = 29%.

map were characterized from mean values followed by the standard deviation noted "$\pm$". The third indicator concerns the grain boundary disorientation divided into intervals as follows:

- low-angle grain boundaries (LAGBs) for angles between 5° and 15°,
- medium-angle grain boundaries (MAGBs) for angles from 15° to 40°,
- high-angle grain boundaries (HAGBs) for angles above 40°.

The advantages of using these three indicators is that they can be simultaneously measured from EBSD mapping and that their combination allows a quantitative description of the evolution from the pearlitic to WEL microstructure.

3. Results

3.1. Indicators and evolution stages

Observations of the WEL microstructure and the microstructures at different degrees of transformation have been previously published in the literature [3,6,32,36]. On the basis of these previous findings as well as the observations made in the present study, five stages were identified from the microstructural gradient (Fig. 3). Fig. 3 displays a longitudinal cross-section of worn pearlitic rail with evidence of WEL formation [1]. A homogeneous WEL is observed to occupy the first 20 μm of the surface (Z = 1). Then, there is a small area of a few micrometers composed of nanostructured grains with few fibers (Z = 0.75). Finally, below the highly fragmented zone, the grains are deformed and appear increasingly less fragmented as the depth increases (Z varies from 0.5 to 0.25 in this zone) over approximately 50 μm. For each stage, the value of Z is given, and the values of the selected microstructural indicators (grain size, aspect ratio, and angular disorientation) were measured from EBSD maps taken at different

depths of a longitudinal cross-section sample from the previous campaign (see Table 2, #Reference test). The details of the different stages will be discussed in the following sections.

3.1.1. As-received and unfragmented pearlitic grains (Z = 0)

In its initial state, the microstructure consists of pearlitic grains with a diameter measured to be approximately 9.6 ± 8.1 μm. This rather small diameter compared to the microstructure presented in Fig. 4-b can be explained by the choice of 5° for the maximum internal disorientation angle. As a result, the measurement reflects the size of pearlite colonies rather than pearlitic grains. In this type of microstructure, the aspect ratio is approximately 2.0 ± 0.9, meaning that these colonies are rather globular in shape. A weakly disoriented state is observed with 30% LAGBs, a majority of MAGBs (40%), and 30% HAGBs.

3.1.2. Fibered and unfragmented grains (Z = 0.25)

The first microstructural change is the start of grain fibration with some fragmentation. At this stage, there is an anisotropy in the deformation of pearlite that depends on the initial orientation of the grains with respect to the shear direction [55,56]. If the grains are preferentially oriented, they will be drawn and oriented in the rolling direction. In the opposite case, they will tend to fragment. Fig. 5 highlights this microstructural stage observed at 60 μm from the rail surface of the sample considered as a reference (see Table 2 for the test conditions of #Reference). The grains orient themselves in the sliding direction and the mean grain size begins to decrease (0.6 ± 0.3 μm). Moreover, the grains are very elongated with an aspect ratio twice as large as in the initial state (4.1 ± 2.7). The proportion of LAGBs begins to decrease from 30% to 20% in favor of MAGBs, which increase and become predominant (48%). The proportion of HAGBs slowly increases from 29% to 32%. A slight increase in hardness of approximately 100 HV has also been reported by several authors [8,26].
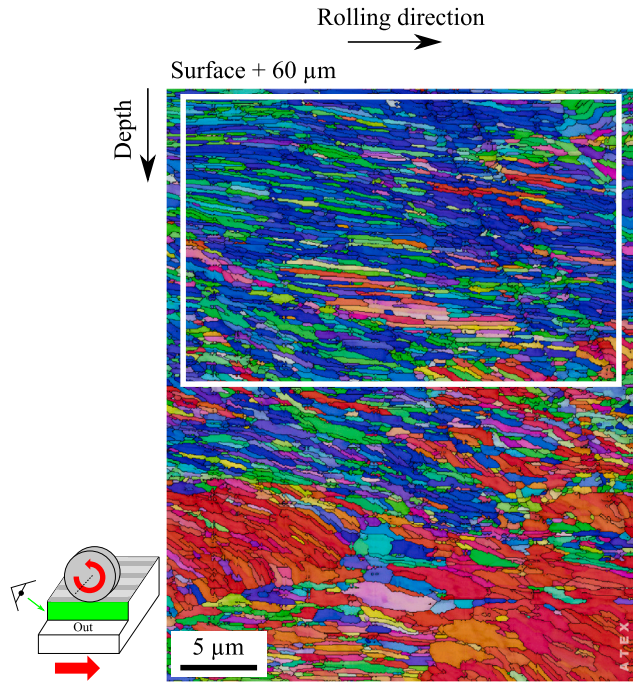
Rolling direction

Surface + 60 μm

Depth

5 μm

Fig. 5. EBSD IPFZ map of a representative fibered grain stage with the presence of very elongated grains located 60 μm from the rail surface of the sample considered as a reference (see Table 2 for the test conditions of #Reference). The white box corresponds to the beginning of the grain fibering (step size = 0.05 μm). Indicators: grain size = 0.6 ± 0.3 μm, aspect ratio of 4.1 ± 2.7, and grain-disorientation repartition: LAGBs = 20%, MAGBs = 48%, and HAGBs = 32%.

3.1.3. Fibered and highly fragmented grain (Z = 0.5)

The accumulation of additional cycles will generate increasingly more dislocations in the grains, which will lead to the initiation of their fragmentation. The grains are fibered and fragmented (Fig. 6). Two types of grain stretching depending on the initial orientation of the grains are observed. The preferentially oriented grains that were elongated in the previous stage begin to fragment; however, an apparent optical and crystallographic fibrous structure remains. The fragmented grains possess the same crystallographic orientation as the initial stretched grain. The grains initially not oriented in the rolling direction have already been fragmented in the previous stage and can form new fibers from the fragmented grains.

Fig. 6 highlights this microstructural stage observed at 20 μm from the rail surface of the sample considered as a reference (see Table 2 for the test conditions of #Reference). At this depth, the new grains are either globular or elongated leading to the decrease of the aspect ratio from 4.1 to 2.8. The grain size becomes more homogeneous, with a mean grain size of 0.6 ± 0.4 μm. The grain disorientation is close to that in the previous stage with 19% LAGBs, 50% MAGBs, and 31% HAGBs.

3.1.4. Unfibered and nanostructured grains (Z = 0.75)

Once entirely fragmented, the grains begin to have a random crystallographic orientation. Fig. 7 highlights this microstructural stage observed at 2 μm from the rail surface of the sample considered as a reference (see Table 2 for the test conditions of #Reference). In the area close to the surface, the microstructure tends to homogenize, and the grain size decreases to a few hundreds of nanometers (0.2 ± 0.1 μm). At this stage, the grains become strongly disoriented, the proportion of LAGBs becomes insignificant (9%) in favor of MAGBs and HAGBs whose proportions are quite close (48% and 43% respectively). The initial grains and cementite lamellaes are no longer optically distinguishable; however, the appearance is still distinguishable from that of a WEL zone. At this stage, the kinetics of the cementite dissolution is assumed to be important; however, the proportion dissolved is insufficient to qualify this stage as a WEL structure. This stage will be called the "nanostructured without fibering" stage. This stage is usually qualified as a "strongly work-hardened", "severely deformed", or "nanocrystalline" state. It is accompanied by a strong increase in hardness, which doubles with respect to that of the initial stage (between 500 and 700 HV) [33,36,57,58].

3.1.5. WEL stage (Z = 1)

The final stage (Z = 1) is the WEL stage characterized by a white appearance with a strong contrast with the pearlitic grains in the subsurface after Nital etching (Fig. 8-a). Optical observation of WELs is then limited to the resolution of optical microscopes, which can only detect areas greater than 1 μm in thickness. An analysis of a WEL patch at the surface of a worn rail in an area prone to developing squats [1] is presented in Fig. 8, with the optical micrograph of the WEL (Fig. 8-a) and the corresponding EBSD IPFZ map (Fig. 8-b). The microstructure consists of fine, very disoriented grains (61% HAGBs) of some hundreds
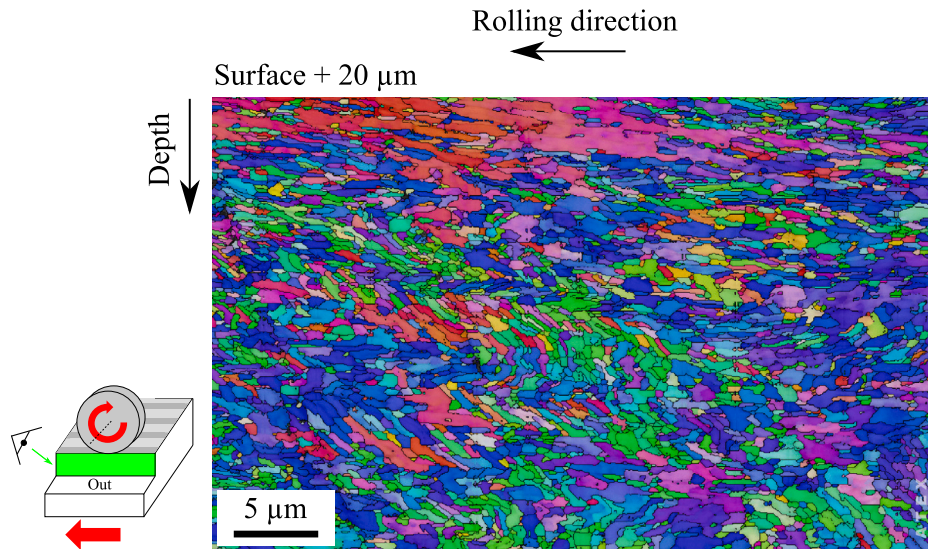

Rolling direction

Surface + 20 μm

Depth

5 μm

Fig. 6. EBSD IPFZ map of a representative fibered and fragmented zone located at 20 μm from the rail surface of the sample considered as a reference (see Table 2 for the test conditions of #Reference) (step size = 0.06 μm). Indicators: grain size = 0.6 ± 0.4 μm, aspect ratio of 3.2 ± 1.7, and grain-disorientation repartition: LAGBs = 19%, MAGBs = 50%, and HAGBs = 31%.
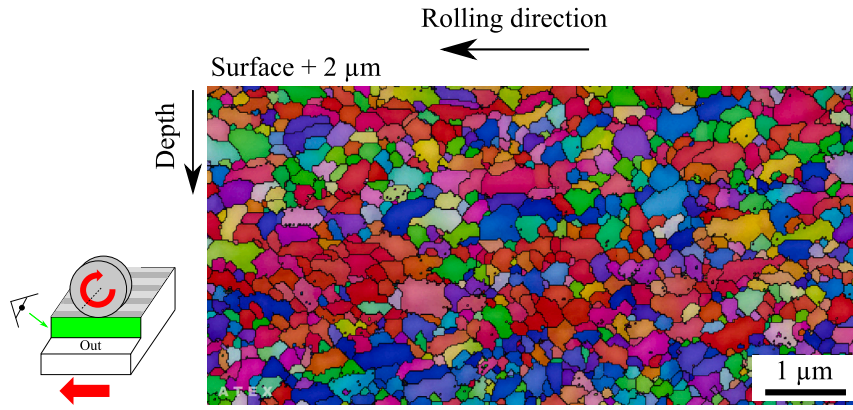
Fig. 7. EBSD IPFZ map of a representative very fragmented grain with the disappearance of fibrous grain in the few micrometers from the rail surface of the sample considered as a reference (see Table 2 for the test conditions of #Reference) (step size = 0.02 μm). Indicators: grain size = 0.2 ± 0.1 μm, aspect ratio = 1.7 ± 0.7, and grain-disorientation repartition: LAGBs = 9%, MAGBs = 48%, and HAGBs = 43%.
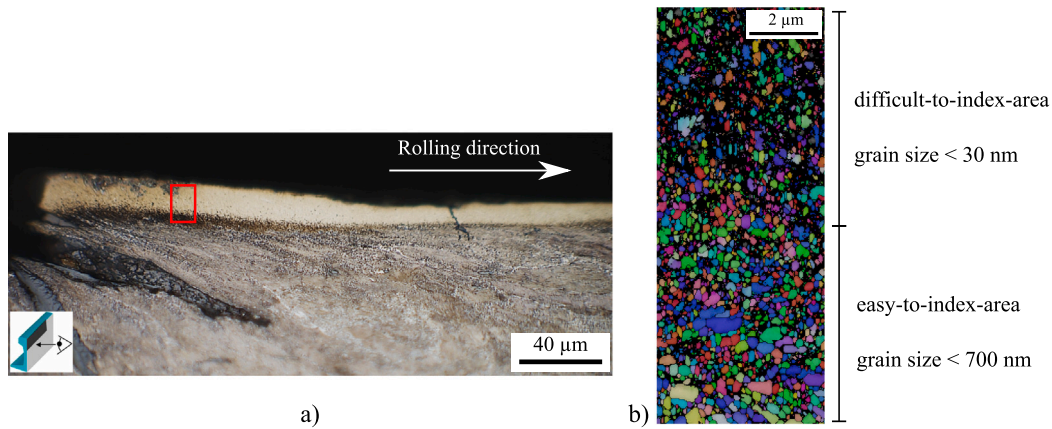

Fig. 8. (a) Optical micrography image showing a WEL patch at the surface of a worn rail in an area prone to developing squats [1]. (b) EBSD IPFZ map of the area shown in the red box, revealing the presence of nanometric grains (step size = 0.03 μm). Indicators: grain size = 0.2 ± 0.1 μm, aspect ratio of 1.6 ± 0.5, and grain-disorientation repartition: LAGBs = 20%, MAGBs = 18%, and HAGBs = 61%.

Table 3
Summary of indicators according to the stages of evolution from the pearlitic state to the final WEL state.

Grain state	Z value (-)	Grain size (μm)	Aspect ratio (-)	LAGB - MAGB - HAGB (%)
As-received pearlitic	0	9.6 ± 8.1	2.0 ± 0.9	30 - 41 - 29
Fibered and unfragmented	0.25	0.6 ± 0.3	4.1 ± 2.7	20 - 48 - 32
Fibered and highly fragmented	0.5	0.6 ± 0.4	2.8 ± 1.4	19 - 50 - 31
Unfibered and nanostructured	0.75	0.2 ± 0.1	1.7 ± 0.7	9 - 48 - 43
WEL	1	0.2 ± 0.1	1.6 ± 0.5	20 - 18 - 61

of nanometers or even less (mean grain size of 0.2 ± 0.1μm) and a globular feature (aspect ratio below 2). The evolution of the microstructure lies in the proportion of cementite dissolution and redistribution of carbon atoms [37]. In the WEL zones, the carbon migrates into the ferritic lattice, grain boundaries, and defects or remains present in a spherical cementite form [3,18,52] . The distinction between the previous state and the WEL stage is not possible from EBSD maps and shall be made from optical image analysis.

3.1.6. Synthesis

The evolution of the microstructural indicators with respect to the stages of WEL transformation is summarized in Table 3. The transition from one state to another is characterized by significant changes in the evolution of one or more indicators.

In the early stages of transformation (from the undeformed pearlitic grains to fibered grains, i.e., Z between 0 and 0.5), the aspect ratio drives the Z evolution as the grain size and grain disorientation evolve relatively slowly.

Then, when the fibration disappears (Z between 0.5 and 0.75), the grains become globular so the aspect ratio remains stable while the grain size decreases drastically. The grain fragmentation combined with the accumulation of deformation increases the disorientation of the grains.

Finally, the transition from the non-fibered and nanostructured grain to the WEL state (Z between 0.75 and 1) consists of a continuous reduction in grain size and a strong increase in grain disorientation.

3.2. Correlation Z vs. grain size

Monitoring of the aspect ratio and grain-boundary disorientation allows the different stages of microstructure evolution to be distinguished. However, their evolution is not a monotonic function, and the variation ranges are not significant enough to formulate a correlation function that explicitly depends on these indicators. In contrast, the grain size decreases exponentially with the stages of microstructure
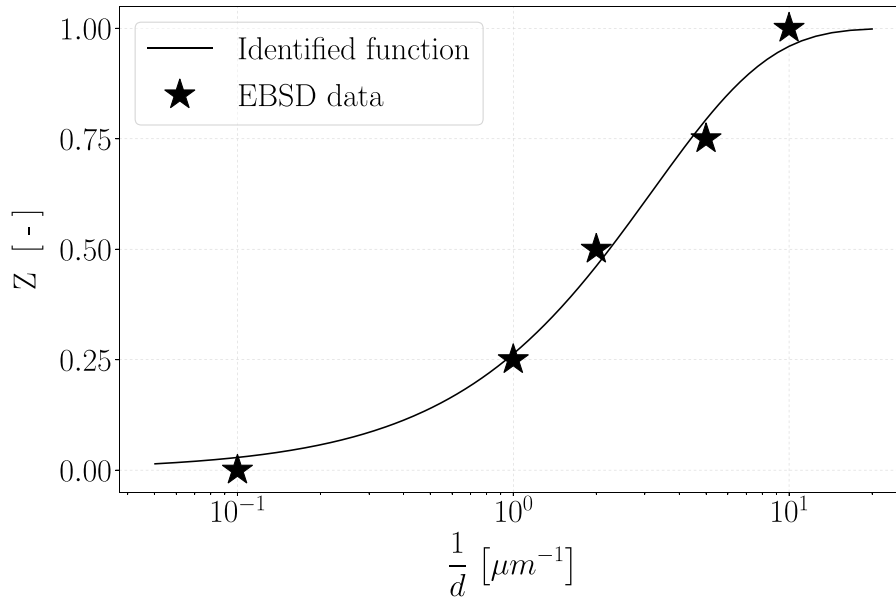
Fig. 9. Correlation function between Z and the grain size based on Eq. (3). This function was identified with the reference data of Table 4. The identified parameters are $d_c = 0.31$ μm and n = 1.02.

Table 4
Reference data used to identify the parameters of the correlation function.

Grain state	Z value (-)	Mean grain size (μm)
As-received pearlitic	0	10
Fibered and unfragmented	0.25	1
Fibered and highly fragmented	0.5	0.5
Unfibered and nanostructured	0.75	0.2
WEL	1	0.1

evolution. A correlation function that depends only on the latter is thus proposed (Eq. (3)):

$$Z = 1 - \exp\left[-\left(\frac{d_c}{d}\right)^n\right] \qquad (3)$$

The analyses of the reference EBSD maps provide information for each stage of microstructure evolution. Table 4 summarizes the grain size and associated stages. The value has been modified for the "fibered and unfragmented" stage (Z = 0.25) because the exact state before the beginning of fragmentation is difficult to obtain. The grain size was then arbitrarily fixed to 1 μm for this stage. Moreover, the final mean grain size is assumed to be lower than 0.1 μm; thus, a value of approximately 0.1 μm was selected. From these reference data, the parameters of the correlation function, d_c and n, were then identified by applying an optimization algorithm (least-squares method). The values of the obtained parameters and the curve of the correlation function identified are shown in Fig. 9. This curve will be used later for validation of the proposed methodology. Notably, from this correlation function, if the grain size is greater than 10 μm, then Z will be close to 0. In contrast, if the grain size is less than 0.1 μm, then Z will tend towards 1 (Fig. 9).

3.3. Experimental results for more critical test conditions

Previous studies have demonstrated the ability of the test bench to obtain microstructures close to that of the WEL without reaching it [33]. New experiments were then performed considering more critical wheel–rail contact conditions related to more severe traffic cases. An increase in contact pressure that would reflect a loaded train under heavy traffic was considered (contact pressure of 1.3 GPa for test #4 and #5). In addition, the sliding ratio was increased from 0.5% to 1.5%

(test #3) to simulate bad weather conditions for example (see Table 2 for more details on the contact conditions).

Fig. 10 summarizes the results obtained for each of the contact conditions given in Table 2. For each test, an optical micrography image of a longitudinal cross-section highlights the gradient of the microstructure and the presence (or absence) of a WEL on the surface. In addition, an optical estimation of Z is given for the microstructure for the first few micrometers of the surface.

First, the experiments performed in the current study reveal the significant effect of slip on the deformation of the grains, which appears more sheared as slip increases. A zone of non-fibrous nanograins can be observed on the surface; however, this does not mean that it is a WEL. It is then an advanced stage with a Z value higher than 0.75 (tests #2 and #3).

In addition, the increase of the contact pressure led to the formation of a WEL for conditions without slip (test #4) and with a slip of 0.5% (test #5). For the rolling-condition test (test #4), the surface is strongly strain-hardened with no apparent longitudinal fibering on the surface and some WEL islands observed. An additional slip rate with the same contact pressure as test #4 (test #5) led to fibering of the grains and a layer of nanograins similar to that observed in the WEL stage covering almost the entire sample surface with a thickness of approximately ten micrometers.

These experimental results demonstrate the combined role of the sliding rate and contact pressure in WEL formation. The effect of the contact conditions on the kinetics of WEL formation will be discussed using numerical simulations (Section 3.3.1). The correlation function identified in Section 2.3 will be applied to two EBSD maps to validate the correlation function (Section 3.3.2).

3.3.1. Validation of the kinetics of Z (numerical simulations)

Rolling and sliding contacts introduce a complex thermomechanical coupling that renders difficult the close modeling of the first micrometers of the surface. The variation of the contact conditions applied (contact pressure and sliding ratio) leads to local variations of the stress tensor and temperature (Fig. 15). Several numerical simulations were conducted to qualitatively compare the observed experimental tendencies. Several assumptions were made:

- The thermomechanical loading of the rail during its history is modeled by a cyclic loading (sinusoidal function) composed of
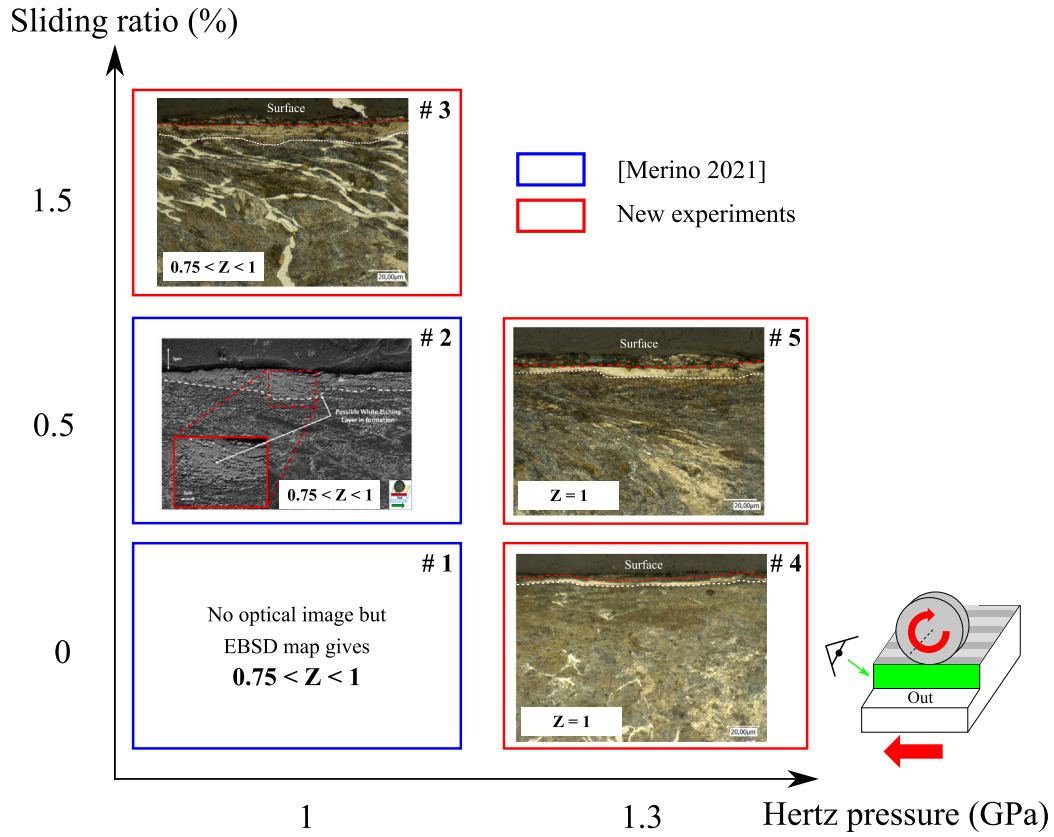
Fig. 10. Synthesis of the results of tests performed for different contact conditions (contact pressure and sliding ratio) on the WEL formation. Each image represents an optical micrograph of a longitudinal cross-section of the ring surface.
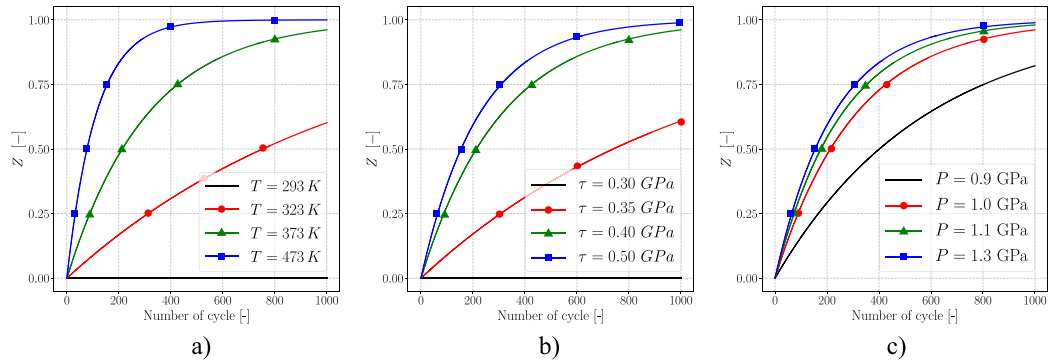

Fig. 11. Effect of thermomechanical loading on WEL formation kinetics: a) #SIMU1: effect of temperature (P = 1 GPa and τ = 0.4 GPa), (b) #SIMU2: effect of von Mises stress (P = 1 GPa and T = 373 K), and (c) #SIMU3: effect of hydrostatic pressure (τ = 0.4 GPa and T = 373 K).

three fields that vary simultaneously from 0 to their maximum value (hydrostatic pressure, von Mises stress, and temperature). One cycle corresponds to the contact time for one wheel passage, and was set to 0.0004 s corresponding of a train rolling at an average speed of 100 km.h^{-1} [59].

- The parameters of the function $g\left[P(t), \sigma_{eq}(t), T(t)\right]$ that governs the kinetics of WEL formation (Eq. (2)) are set to be favorable for WEL formation under the imposed conditions. The numerical values of these parameters are given in Appendix.
- The differential equation governing the WEL formation kinetics (Eq. (2)) is solved by finite differentiation considering a time step small enough to converge to the exact solution.

Three series of tests are presented to illustrate the sensitivity of the model to the temperature (#SIMU1), von Mises stress (#SIMU2), and

hydrostatic pressure (#SIMU3). The details of the test conditions for each series are given in Table 5.

First, the effect of temperature (fixed hydrostatic pressure and von Mises stress) after 1000 cycles was studied (#SIMU1, Fig. 11-a). For a temperature of 293 K, the material remains in the pearlitic state (Z = 0). For a higher temperature of 50 K (323 K), it reaches an advanced stage, and the grains become fibered and fragmented (Z = 0.65). Finally, if the temperature exceeds 373 K, the material will be completely transformed into a WEL (Z = 1) after 1000 cycles. For the second series of tests (#SIMU2), the shear stress effect was studied (fixed hydrostatic pressure and temperature). After 1000 cycles, the material does not change for a shear stress of 0.3 GPa (Fig. 11-b). The material starts to transform from a shear stress between 0.3 and 0.35 GPa. For a shear stress higher than 0.4 GPa, the material reaches a nanostructured stage very close to the WEL stage (Z > 0.96).
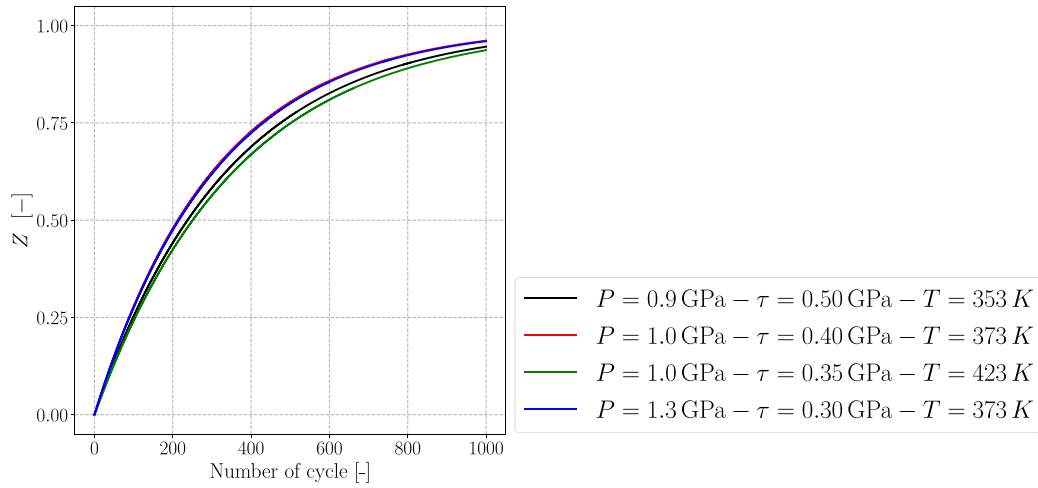
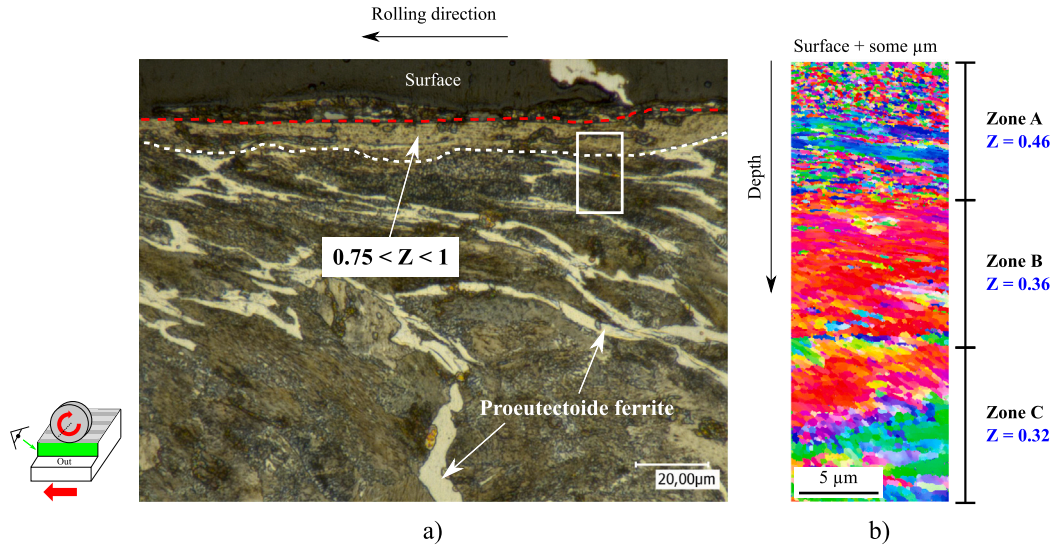**Fig. 12.** Identical WEL formation kinetics obtained from different thermomechanical stresses (#SIMU4).

a)

b)

Fig. 13. Gradient of transformation of the microstructure of a longitudinal cross-section of test #3 (P = 1 GPa; γ = 1.5%; N_{cycle} = 1000 cycles): (a) optical image after Nital etching, the first 30 micrometers correspond to a stage close to that of WEL. Z is optically estimated to be greater than 0.75. (b) IPFX map of the first 30 micrometers of the surface (step size = 0.05 μm). The map was divided into three parts to numerically estimate the Z value from the average grain size in each area.

Table 5
Test conditions for the numerical simulations (#SIMU1, #SIMU2, and #SIMU3).

Simulation reference	P (GPa)	τ (GPa)	T (K)
#SIMU1	1	0.4	293 - 323 - 373 - 473
#SIMU2	1	0.3 - 0.35 - 0.4 - 0.5	373
#SIMU3	0.9 - 1 - 1.1 - 1.3	0.4	373

Finally, the third set of tests (#SIMU3) also illustrates the effect of hydrostatic pressure on the transformation kinetics of WEL formation (Fig. 11-c). For a higher pressure, the material reaches the unfibered and nanostructured stage (Z = 0.75) more rapidly. Indeed, this stage is reached after 300 cycles for a pressure of 1.3 GPa, whereas 800 cycles are necessary for a pressure of 0.9 GPa.

The last series of tests (#SIMU4) illustrates that the same kinetics of WEL formation is achieved for different sets of contact conditions (Table 6). For example, for a temperature of 373 K, a combination (hydrostatic pressure; shear stress) of (1 GPa; 0.4 GPa) is equivalent to (1.3 GPa; 0.3 GPa) in terms of WEL formation kinetics (Fig. 12).

Numerical simulations show that the WEL kinetics model is sensitive to hydrostatic pressure, shear stresses, and temperature. These simulations demonstrate that the more intensive contact conditions will

Table 6
#SIMU4: Test conditions for the last series of tests leading to the same kinetics of Z.

P (GPa)	τ (GPa)	T (K)
0.9	0.5	353
1	0.4	373
1	0.35	423
1.3	0.3	373

accelerate the formation of WELs and validate the assumptions of the previously proposed model. Furthermore, it is numerically possible to reproduce the same WEL formation kinetics despite a different loading history. In other words, the presence of a WEL after a given number of cycles may be the result of different thermomechanical conditions.
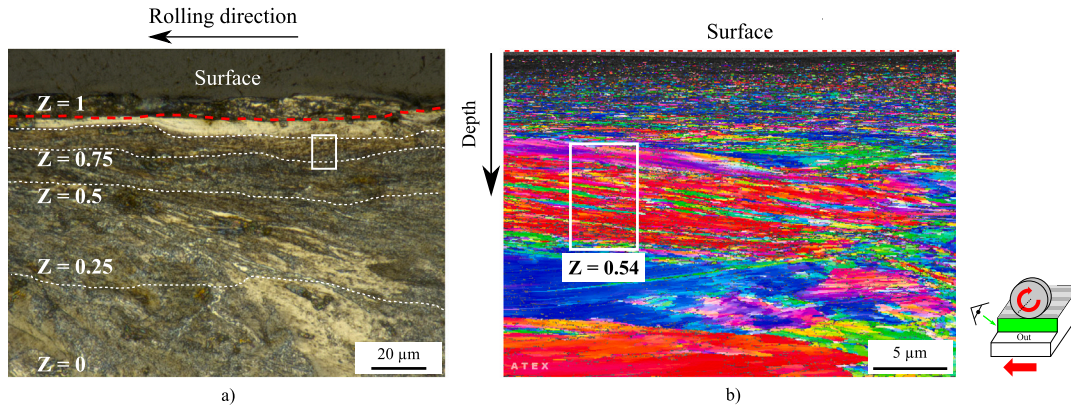
Fig. 14. Longitudinal cross-section of the ring for test #5 (P = 1.3 GPa; γ = 0.5%; N_{cycle} = 1000 cycles): (a) optical micrograph after Nital etching with estimation of the z-gradient by optical scanning; (b) IPFX map obtained at another location of the sample from the surface, which is homogeneous over the whole surface (fragmented, non-fibrous) with partial WEL islands. Step size of indexation of 0.05 µm. The grains are very flattened and poorly indexed over the first 6 micrometers. Indicators: grain size = 0.4 ± 0.1 µm, which corresponds to Z = 0.54; aspect ratio = 8.9 ± 3.8; and LAGB = 68% - MAGB = 25% - HAGB = 7%.
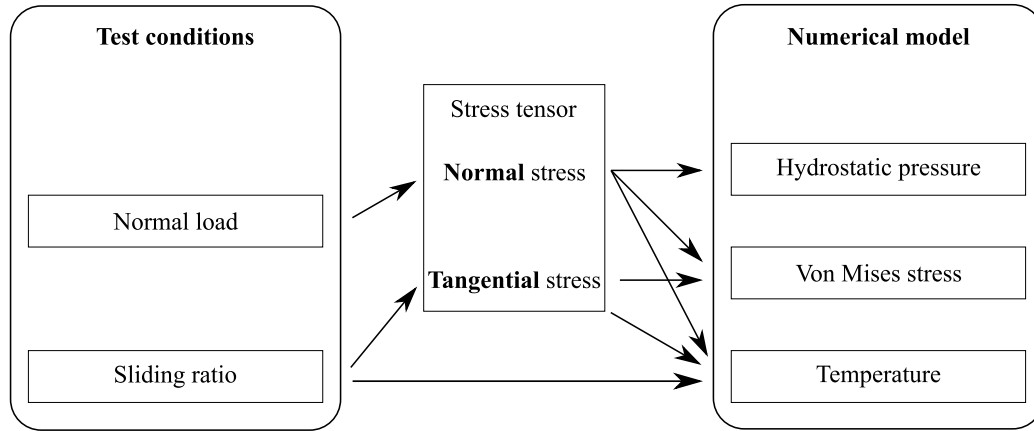

Fig. 15. Scheme of the effects of the sliding ratio and contact pressure on the stress tensor and temperature in the rail surface.

Table 7
Summary of measurements of indicators for each part of the EBSD map (Fig. 13-b).

Zone	Grain size (µm)	Aspect ratio	LAGB - MAGB - HAGB (%)	Z (optical estimation)	Z (model)
A	0.5 ± 0.03	1.4 ± 0.1	7 - 40 - 53	[0.5 ; 0.75]	0.46
B	0.7 ± 0.4	5.5 ± 2.6	27- 45 - 28	[0.25 ; 0.5]	0.36
C	0.8 ± 0.8	2.8 ± 1.3	56 - 38 - 6	[0.25 ; 0.5]	0.32

These results are consistent with the experimental results on the effect of contact pressure and sliding ratio.

3.3.2. Application of the correlation function with EBSD map

The surface of two samples from tests #3 and #5 were characterized using EBSD (Figs. 13 and 14) to validate the methodology proposed in this study. For each map, the values of the indicators were measured. In particular, the average grain size was used to obtain an estimate of the internal variable Z calculated from the correlation function identified.

First validation test (#3)

This first validation test concerns the most important slip conditions of the experimental study (γ = 1.5%). Fig. 13 shows a longitudinal cross-section of the ring tested surface with an optical image after Nital etching (Fig. 13-a) and an IPFZ figure (Fig. 13-b). Fig. 13-a highlights the microstructural gradient over 40 µm from the surface. In the first 10 µm, a transformed zone close to the WEL stage is observed (Z between 0.75 and 1). Then, strongly sheared proeutectoid pearlite grains are observed over approximately 30 µm (Z between 0.25 and 0.75). Because the grains are initially eutectoid, the presence of

proeutectoid ferrite reveals a possible increase of temperature due to the severe slipping condition.

The microstructural gradient of the first 30 µm was then investigated using an EBSD map (Fig. 13-b) with measurements of the three indicators. The map was divided into 3 zones referenced as A, B, and C. The microstructural indicators measured in each zone are summarized in Table 7.

The mean grain size decreased upon approaching the contact surface (0.5 µm for zone A, 0.7 µm for zone B, and 0.8 µm for zone C). Moreover, there was also an increase of the grain disorientation. In fact, the HAGBs were predominant in zone A (53%), and the proportion was the lowest in zone C (6%). Finally, the evaluation of the aspect ratio reveals that the grains were the most elongated in zone B (aspect ratio of 5.5). The aspect ratio in zone A is close to 1 and confirms the quasi-spherical grain shape in this area.

All these observations allow the potential microstructural stage, and thus a Z value for each area, to be estimated. The grains of zone A were optically fibered and probably fragmented; thus, Z was between 0.5 and 0.75. In zones B and C, the grains appeared less fragmented and were fibered; thus, Z was between 0.25 and 0.5 (Table 7).

Table 8
Summary of measurements of indicators for the white box in the EBSD map (Fig. 14-b).

Grain size (µm)	Aspect ratio	LAGB - MAGB - HAGB (%)	Z (optical estimation)	Z (model)
0.4 ± 0.1	8.9 ± 3.8	68 - 25 - 7	$Z > 0.5$	0.54

The Z correlation function defined and identified in Section 3.2 was applied to this map with consideration of the grain-size measurements for each area separately. The results are in a good agreement with the previous estimation: for zones A, B, and C, Z was computed to be 0.46, 0.36, and 0.32, respectively.

Second validation test (#5)

This second validation test (#5) concerns the most important pressure conditions (P = 1.3 GPa) with a small sliding ratio ($\gamma = 0.5\%$). Fig. 14 shows a longitudinal cross-section of the ring surface tested with an optical image after Nital etching (Fig. 14-a) and an IPFZ map (Fig. 14-b).

Fig. 14-a highlights the microstructural gradient over 60 µm from the surface. In the first 5 µm, a WEL zone was successfully reproduced (Z = 1). Then, below the totally transformed area, the grains appeared very fragmented and fibered over 20 µm (Z between 0.5 and 0.75). Finally, a fibered area, less (or not) fragmented extended over 35 µm (Z between 0.25 and 0.5). The first 30 µm observed by EBSD confirm that the grains were very fragmented, elongated, and compressed (Fig. 14-b). Despite the low step size of indexation (0.05 µm), the first 5 µm (WEL area) could not be indexed, indicating very small and deformed grains in this region. Another area was characterized with a smaller step size of 0.015 µm (white box in the EBSD map in Fig. 14). The indicators were measured in this area assumed to be in an advanced stage close to WEL ($Z > 0.75$). In fact, the grain size of 0.4 ± 0.1 µm leads to a Z value of 0.54. The mean aspect ratio was close to 9 in this zone, confirming that the grains were very elongated and also compressed. Moreover, the grain disorientation was very low (majority of LAGBs with 68%) despite the advanced stage of transformation.

The unexpectedly high values of the latter two indicators can be explained by a high level of compressive stress compared to previous tests, which would reduce the disorientation of the grains and their rather elongated shape despite their small size. The grains were much more compressed than in the previous tests, which could explain the difficulty in indexing the first micrometers of the surface. These results confirm that the grain size could be used to track the microstructural evolution and that the disorientation and the aspect ratio are not the most relevant indicators for the WEL formation.

4. Discussion

4.1. Relevance of microstructural indicators

Three microstructural indicators were considered for monitoring of the evolution stages of WEL formation. During the WEL formation process, the grain size decreases drastically by a factor of 10–100 locally. Thus, it is a good indicator to describe the kinetics of WEL formation.

Nevertheless, because of the small grain size, indexation is difficult and the EBSD map alone does not allow the presence or absence of a WEL to be distinguished. An optical micrograph of the zone is thus necessary to verify the presence of a WEL. Grain size measurement alone does not provide information on either the evolution stage of the grains or the loading history of the rail.

These ambiguities can be overcome by measuring the other two indicators: the aspect ratio and grain disorientation. In fact, the aspect ratio allows the first steps of WEL formation (grain stretching) to be described numerically. During those stages ($Z < 0.5$), the aspect ratio greatly increases until an assumed maximum value. At this stage, Z is equal to 0.25. Then, the most fibered grains begin to fragment, and

the aspect ratio decreases until reaching a value close to 1 because the grain shape tends to stabilize (Z = 0.75).

Finally, the repartition of the grain disorientation alone does not allow the evolution stage to be distinguished because it clearly depends on the loading history, especially for extreme cases. Indeed, for a high degree of sliding ($\gamma = 1.5\%$, test #3), there is a clear tendency of increased grain disorientation during the grain-size reduction. This increased grain disorientation could be due to a high level of shear stresses (Table 7). In contrast, for the test with the highest contact pressure (P = 1.3 GPa, test #5), the grain disorientation was surprisingly low even for the nanostructured grains (Table 8). This result is probably due to high compressive stresses. Moreover, the aspect ratio of the compressed grains was very high compared to the values of the indicators used as reference data (Table 4).

This study reveals the necessity of using optical micrography to first approximately determine the microstructural gradient size. Then, the combined measurements of the grain size, aspect ratio, and grain disorientation permit the different stages of WEL formation to be distinguished. Their combination provides more information about the loading history of the rails. Regardless of the type of loading, WEL formation always results from a high reduction in grain size, thus explaining the choice of a correlation function that depends on the grain size to relate experimental data and the model. The two other indicators provide information on the loading history of the rail.

A last remark concerns the high heterogeneity of the material and thus the heterogeneity of the indicator values, which are mean values of the grain distribution (grain size and shape). Taking into account the statistical distribution of grains would be an important improvement to more accurately describe the global behavior of the material. However, the choice was made to remain in a framework accessible at reduced cost.

4.2. Effect of the test conditions on the kinetics of WEL formation

More extreme conditions were tested to determine the possibility of using the test bench to reach levels of transformations closer to those of WELs. The combined role of slip and contact pressure in WEL formation is discussed in this section, highlighting their different effects on the thermomechanical field (Fig. 15). In fact, it is very difficult to determine the stress tensor and temperature on the contact surface because of the effect of the local contact dynamics (roughness [60], 3rd body [61]). The effects of the two test parameters are summarized in Section 4.2.1 (effect of the sliding ratio) and Section 4.2.2 (effect of the contact pressure) to relate to the numerical model (Section 4.2.3).

In addition, there are also transverse forces due to the nature of the ring-roller contact. In fact, Merino [33] and Lafilé [34] observed the transverse cross-sections of the ring that revealed a strain gradient even for pure rolling conditions. However, in those conditions, no WEL were observed.

4.2.1. Effect of the sliding ratio

Contrary to the real contact conditions, the sliding ratio induced in the experiments allows better control of the contact conditions. The contact zone is generally divided into sliding and sticking zones that depend on the sliding ratio [62–66]. If the sliding ratio is high enough, the contact zone is in total full slip. It is assumed that the experiments presented in this paper were performed under those conditions (sliding ratio between 0% and 1.5% and contact pressure between 1 and 1.3 GPa).

With this assumption, several explanations can be provided. First, the sliding ratio has a direct effect on the contact temperature [67–69]. Numerical simulations of the wheel–rail contact, without lateral forces have shown that for a slip of 2.38%, the temperature does not exceed 573 K [70]. This trend has also been confirmed in other studies [69,71], which allows us to give an order of magnitude of the temperature of contact, which would be between 293 K and 673 K. Under the conditions tested, with the total maximum sliding of 1.5%, the formation of purely thermal WEL is unlikely. Moreover, a WEL has been produced for much lower slip levels, which justifies predominantly mechanically-induced WEL formation assisted by temperature. Indeed, a moderate increase of temperature could catalyze the kinetics of cementite dissolution [23,72]. Thus, it can be unambiguously stated that temperature is rather secondary in the formation of the WELs reproduced in this study. Nevertheless, for higher sliding ratio, the contact temperature will no longer be assumed to be negligible compared to the mechanical loading. Therefore, thermally-induced WEL formation might occur above a critical sliding ratio.

The second effect of the sliding ratio is on the tangential stress, which is saturated when the contact zone is in total sliding (Coulomb friction law). Under that condition, the maximal tangential stress τ_{max} is proportional to the friction coefficient μ_0 times the maximum contact pressure P_{max} (Eq. (4)).

$$\tau_{max} = \mu_0 \times P_{max} \qquad (4)$$

Therefore, for low values of sliding ratio ($\leq$ 1.5%), the tangential stress is saturated; for a higher sliding ratio, the shear strain is higher. These conditions could facilitate the first stage of WEL formation (grain fibration) compared to the case without sliding.

4.2.2. Effect of the contact pressure

The contact pressure has shown a real effect on WEL formation even without sliding (Fig. 10). It has many effects on the stress tensor and temperature [67]. The high contact pressure applied (1 or 1.3 GPa) induces a high hydrostatic pressure in the contact zone and also a high von Mises stress that drives the kinetics of plasticity of the material.

Moreover, the increase of the contact pressure combined with the sliding ratio of 0.5% also contributes to the development of a more significant maximal tangential stress (Eq. (4)). In fact, if we compare experiments #2 and #5, an increase of 30% in the maximal contact pressure P_{max} will theoretically lead to an increase of 30% in the maximal tangential stress τ_{max}. This could therefore explain why the microstructure on the surface of test #5 is the closest to that of the WELs observed on worn rails.

Such a level of nanostructuring would then be possible through the multiaxial mechanical loading combining tangential stresses (longitudinal and transverse) and hydrostatic pressure. The latter makes metals (and steels in particular) more ductile [73–76] and could facilitate the deformation and transformation of grains before cracking. Indeed, high pressure torsion tests (HPT) of pearlitic steels [30] allow very high levels of shear plastic strain without failure and lead to cementite dissolution. Although the loading history differs between HPT tests and the triboring test bench, in both configurations, the material can be considered to be locally subjected to a high hydrostatic pressure (contact pressure effect) combined with a high shear (combined effect of contact pressure and slip ratio). The combination of these two factors would then facilitate the transition from the non-fibrous nanostructured stage (Z = 0.75) to the WEL stage (Z = 1).

4.2.3. Correlation between experiments and the model

The results demonstrate that slip and contact pressure effectively contribute to the formation of WELs. In addition, increasing the contact pressure and/or the sliding ratio actually led to the highest kinetics (test #3 and #5). The numerical simulations confirmed these experimental observations, validating the pressure–shear coupling proposed by Thiercelin et al. [43].

Furthermore, it is apparent that the kinetics of WEL formation is not unique, as several test conditions led to WEL formation (test #3 and #5 in Section 3.3.2). The significant result is that WEL formation is possible for different loading paths, which demonstrates a non-unique formation scenario. These results were also successfully captured numerically (Fig. 12 in Section 3.3.1).

5. Conclusions and perspectives

Using experimental data, three microstructural indicators were chosen to describe the formation of mechanical WEL: the grain size, the aspect ratio and the grain boundary disorientation. The WEL formation induces a microstructural gradient, that can be described using a variable Z, varying from 0 (undeformed stage) to 1 (WEL stage). A correlation function, that considers the values of the microstructural indicators allows to compute Z for a given microstructure.

Representative wheel–rail contact tests using the Triboring test bench reproduced the mechanical formation of WEL for low slip ratio. In addition, it was experimentally confirmed that the contact conditions leading to WEL formation are not unique as predicted by the numerical model. Therefore, the assumption of a pressure–shear coupling in the WEL formation was validated experimentally.

Future studies are planned to accurately measure the contact temperature as a function of test conditions (contact pressure and slip ratio). Tests for slightly higher slip ratio should be considered to increase locally the contact temperature and to estimate a critical sliding ratio for thermally-induced WEL.

All the proposed methodology was applied to a specific pearlitic steel and could be extended to other pearlitic steel grades to compare to WEL formation kinetics and the evolution of the microstructural indicators under the same contact conditions as presented by Wen et al. using another test bench [36].

CRediT authorship contribution statement

Léo Thiercelin: Conceptualization, Methodology, Software, Investigation, Writing – original draft. **Sophie Cazottes:** Conceptualization, Methodology, Investigation, Resources, Writing – original draft, Supervision. **Pierrick Merino:** Investigation, Experiments, Resources, Writing – review & editing. **Aurélien Saulot:** Conceptualization, Methodology, Resources, Writing – review & editing, Supervision, Project administration. **Frédéric Lebon:** Conceptualization, Methodology, Software, Writing – review & editing, Supervision, Project administration.

Declaration of competing interest

The authors declare that they have no known competing financial interests or personal relationships that could have appeared to influence the work reported in this paper.

Data availability

No data was used for the research described in the article.

Table 9
Set of parameters of the numerical model selected for the simulation.

σ_c (GPa)	τ_c (GPa)	T_c (K)	T_0 (K)	ω_1 (GPa)	ω_2 (GPa)	ω_3 (GPa)	$\frac{\kappa}{\eta}$
30	1	1000	293	1×10^7	1×10^7	1	500

Appendix

The analytical expression of the $g\left[P(t), \sigma_{eq}(t), T(t)\right]$ function in Eq. (5) is recalled from [43]:

$$g\left[P(t), \sigma_{eq}(t), T(t)\right] = \frac{\kappa}{\eta} \left\langle f_{\text{therm}}\left[T(t)\right] - f_{\text{meca}}\left[P(t), \sigma_{eq}(t)\right] \right\rangle \quad (5)$$

where $f_{\text{therm}}\left[T(t)\right]$ (Eq. (6)) and $f_{\text{meca}}\left[P(t), \sigma_{eq}(t)\right]$ (Eq. (7)) represent the thermal and mechanical contributions for the thermomechanical criterion of WEL formation, respectively:

$$f_{\text{therm}}\left[T(t)\right] = \frac{T(t) - T_0}{T_c - T_0} \quad (6)$$

$$
\begin{aligned}
f_{\text{meca}}\left[P(t), \sigma_{eq}(t)\right] &= \frac{\left\langle \exp\left(-\frac{<P(t)>}{\omega_1}\right) - \exp\left(-\frac{\sigma_c}{\omega_1}\right) \right\rangle}{1 - \exp\left(-\frac{\sigma_c}{\omega_1}\right)} \\
&\times \frac{\left\langle \exp\left(-\frac{\sigma_{eq}(t)}{\omega_2}\right) - \exp\left(-\frac{\tilde{\tau}[P(t)]}{\omega_2}\right) \right\rangle}{1 - \exp\left(-\frac{\tilde{\tau}[P(t)]}{\omega_2}\right)}
\end{aligned} \quad (7)
$$

where

$$\tilde{\tau}\left[P(t)\right] = \frac{\left\langle \exp\left(-\frac{\sigma_{eq}(t)}{\omega_3}\right) - \exp\left(-\frac{\tau_c}{\omega_3}\right) \right\rangle}{1 - \exp\left(-\frac{\tau_c}{\omega_3}\right)} \quad (8)$$

where $\kappa, \eta, T_c, \tau_c, \sigma_c, \omega_1, \omega_2$, and ω_3 are the parameters of the model. Their values are given in Table 9 to have a WEL criterion formation under classical wheel–rail contact conditions.

References

[1] S. Simon, A. Saulot, C. Dayot, X. Quost, Y. Berthier, Tribological characterization of rail squat defects, Wear 297 (1–2) (2013) 926–942, http://dx.doi.org/10.1016/j.wear.2012.11.011.

[2] M. Masoumi, E.A. Ariza, A. Sinatora, H. Goldenstein, Role of crystallographic orientation and grain boundaries in fatigue crack propagation in used pearlitic rail steel, Mater. Sci. Eng. A 722 (2018) 147–155, http://dx.doi.org/10.1016/j.msea.2018.03.028.

[3] A. Kumar, G. Agarwal, R. Petrov, S. Goto, J. Sietsma, M. Herbig, Microstructural evolution of white and brown etching layers in pearlitic rail steels, Acta Mater. 171 (2019) 48–64, http://dx.doi.org/10.1016/j.actamat.2019.04.012.

[4] S. Li, J. Wu, R.H. Petrov, Z. Li, R. Dollevoet, J. Sietsma, "Brown etching layer": A possible new insight into the crack initiation of rolling contact fatigue in rail steels? Eng. Fail. Anal. 66 (2016) 8–18, http://dx.doi.org/10.1016/j.engfailanal.2016.03.019.

[5] J. Wu, R. Petrov, S. Kölling, P. Koenraad, L. Malet, S. Godet, J. Sietsma, Micro and Nanoscale Characterization of Complex Multilayer-Structured White Etching Layer in Rails, Metals 8 (10) (2018) 749, http://dx.doi.org/10.3390/met8100749.

[6] B. Dylewski, M. Risbet, S. Bouvier, The tridimensional gradient of microstructure in worn rails – Experimental characterization of plastic deformation accumulated by RCF, Wear 392–393 (2017) 50–59, http://dx.doi.org/10.1016/j.wear.2017.09.001.

[7] J. Bertrand, A. Galtier, N. Guelton, C. Juckum, C. Scott, M. Seux, Phase blanche dans les rails, (MPM 97 N 1126) 1997, p. 37.

[8] P. Clayton, M.B.P. Allery, Metallurgical Aspects of Surface Damage Problems in Rails, Canadian Metallurg. Quart. 21 (1) (1982) 31–46, http://dx.doi.org/10.1179/000844382795243803.

[9] S. Newcomb, W. Stobbs, A transmission electron microscopy study of the white-etching layer on a rail head, Mater. Sci. Eng. 66 (2) (1984) 195–204, http://dx.doi.org/10.1016/0025-5416(84)90180-0.

[10] G. Baumann, H. Fecht, S. Liebelt, Formation of white-etching layers on rail treads, Wear 191 (1–2) (1996) 133–140, http://dx.doi.org/10.1016/0043-1648(95)06733-7.

[11] L. Wang, A. Pyzalla, W. Stadlbauer, E. Werner, Microstructure features on rolling surfaces of railway rails subjected to heavy loading, Mater. Sci. Eng. A 359 (1–2) (2003) 31–43, http://dx.doi.org/10.1016/S0921-5093(03)00327-7.

[12] E. Wild, L. Wang, B. Hasse, T. Wroblewski, G. Goerigk, A. Pyzalla, Microstructure alterations at the surface of a heavily corrugated rail with strong ripple formation, Wear 254 (9) (2003) 876–883, http://dx.doi.org/10.1016/S0043-1648(03)00239-4.

[13] W. Daniel, Final Report on the Rail Squat Project R3-105, CRC for rail innovation, Australia, 2013.

[14] S. Pal, W.J.T. Daniel, C.H.G. Valente, A. Wilson, A. Atrens, Surface damage on new AS60 rail caused by wheel slip, Eng. Fail. Anal. 22 (2012) 152–165, http://dx.doi.org/10.1016/j.engfailanal.2012.01.002.

[15] M. Ishida, Rolling contact fatigue (RCF) defects of rails in Japanese railways and its mitigation strategies, 2013, p. 8.

[16] A. Al-Juboori, D. Wexler, H. Li, H. Zhu, C. Lu, A. McCusker, J. McLeod, S. Pannil, Z. Wang, Squat formation and the occurrence of two distinct classes of white etching layer on the surface of rail steel, Int. J. Fatigue 104 (2017) 52–60, http://dx.doi.org/10.1016/j.ijfatigue.2017.07.005.

[17] A. Kumar, A. Saxena, C. Kirchlechner, M. Herbig, S. Brinckmann, R. Petrov, J. Sietsma, In situ study on fracture behaviour of white etching layers formed on rails, Acta Mater. 180 (2019) 60–72, http://dx.doi.org/10.1016/j.actamat.2019.08.060.

[18] H. Zhang, S. Ohsaki, S. Mitao, M. Ohnuma, K. Hono, Microstructural investigation of white etching layer on pearlite steel rail, Mater. Sci. Eng. A 421 (1–2) (2006) 191–199, http://dx.doi.org/10.1016/j.msea.2006.01.033.

[19] W. Österle, H. Rooch, A. Pyzalla, L. Wang, Investigation of white etching layers on rails by optical microscopy, electron microscopy, X-ray and synchrotron X-ray diffraction, Mater. Sci. Eng. A 303 (1–2) (2001) 150–157, http://dx.doi.org/10.1016/S0921-5093(00)01842-6.

[20] A. Al-Juboori, H. Zhu, D. Wexler, H. Li, C. Lu, A. McCusker, J. McLeod, S. Pannila, J. Barnes, Evolution of rail surface degradation in the tunnel: The role of water on squat growth under service conditions, Eng. Fract. Mech. 209 (2019) 32–47, http://dx.doi.org/10.1016/j.engfracmech.2019.01.018.

[21] A. Al-Juboori, H. Zhu, D. Wexler, H. Li, C. Lu, A.A. Gazder, J. McLeod, S. Pannila, J. Barnes, Microstructural changes on railway track surfaces caused by electrical leakage between wheel and rail, Tribol. Int. 140 (2019) 105875, http://dx.doi.org/10.1016/j.triboint.2019.105875.

[22] R. Nakkalil, Formation of adiabatic shear bands in eutectoid steels in high strain rate compression, Acta Metallurg. Mater. 39 (11) (1991) 2553–2563, http://dx.doi.org/10.1016/0956-7151(91)90070-H.

[23] W. Lojkowski, M. Djahanbakhsh, G. Bürkle, S. Gierlotka, W. Zielinski, H.-J. Fecht, Nanostructure formation on the surface of railway tracks, Mater. Sci. Eng. A 303 (1–2) (2001) 197–208, http://dx.doi.org/10.1016/S0921-5093(00)01947-X.

[24] L. Thiercelin, S. Cazottes, A. Saulot, F. Lebon, F. Mercier, C. Le Bourlot, S. Dancette, D. Fabrègue, Development of Temperature-Controlled Shear Tests to Reproduce White-Etching-Layer Formation in Pearlitic Rail Steel, Materials 15 (19) (2022) 6590, http://dx.doi.org/10.3390/ma15196590.

[25] M. Steenbergen, R. Dollevoet, On the mechanism of squat formation on train rails – Part I: Origination, Int. J. Fatigue 47 (2013) 361–372, http://dx.doi.org/10.1016/j.ijfatigue.2012.04.023.

[26] F. Alwahdi, A. Kapoor, F. Franklin, Subsurface microstructural analysis and mechanical properties of pearlitic rail steels in service, Wear 302 (1–2) (2013) 1453–1460, http://dx.doi.org/10.1016/j.wear.2012.12.058.

[27] W. Tyfour, J. Beynon, The effect of rolling direction reversal on the wear rate and wear mechanism of pearlitic rail steel, Tribol. Int. 27 (6) (1994) 401–412, http://dx.doi.org/10.1016/0301-679X(94)90017-5.

[28] W.R.A. Tyfour, Interaction between Wear and Rolling Contact Fatigue in Pearlitic Rail Steels (Ph.D. thesis), University of Leicester, 1995.

[29] W. Tyfour, J. Beynon, A. Kapoor, The steady state wear behaviour of pearlitic rail steel under dry rolling-sliding contact conditions, Wear 180 (1–2) (1995) 79–89, http://dx.doi.org/10.1016/0043-1648(94)06533-0.

[30] Y. Ivanisenko, W. Lojkowski, R. Valiev, H.-J. Fecht, The mechanism of formation of nanostructure and dissolution of cementite in a pearlitic steel during high pressure torsion, Acta Mater. 51 (18) (2003) 5555–5570, http://dx.doi.org/10.1016/S1359-6454(03)00419-1.

[31] C. He, H. Ding, L. Shi, J. Guo, E. Meli, Q. Liu, A. Rindi, Z. Zhou, W. Wang, On the microstructure evolution and nanocrystalline formation of pearlitic wheel material in a rolling-sliding contact, Mater. Charact. 164 (2020) 110333, http://dx.doi.org/10.1016/j.matchar.2020.110333.

[32] Y. Hu, L. Zhou, H. Ding, R. Lewis, Q. Liu, J. Guo, W. Wang, Microstructure evolution of railway pearlitic wheel steels under rolling-sliding contact loading, Tribol. Int. 154 (2021) 106685, http://dx.doi.org/10.1016/j.triboint.2020.106685.

[33] P. Merino, S. Cazottes, V. Lafilé, M. Risbet, A. Saulot, S. Bouvier, J. Marteau, Y. Berthier, An attempt to generate mechanical white etching layer on rail surface on a new rolling contact test bench, Wear 482–483 (2021) 203945, http://dx.doi.org/10.1016/j.wear.2021.203945.

[34] V. Lafilé, J. Marteau, M. Risbet, S. Bouvier, P. Merino, A. Saulot, Characterization of the Microstructure Changes Induced by a Rolling Contact Bench Reproducing Wheel/Rail Contact on a Pearlitic Steel, Metals 12 (5) (2022) 745, http://dx.doi.org/10.3390/met12050745.

[35] Y. Zhou, J. Peng, W. Wang, X. Jin, M. Zhu, Slippage effect on rolling contact wear and damage behavior of pearlitic steels, Wear 362–363 (2016) 78–86, http://dx.doi.org/10.1016/j.wear.2016.05.001.

[36] J. Wen, J. Marteau, S. Bouvier, M. Risbet, F. Cristofari, P. Secordel, Comparison of microstructure changes induced in two pearlitic rail steels subjected to a full-scale wheel/rail contact rig test, Wear 456–457 (2020) 203354, http://dx.doi.org/10.1016/j.wear.2020.203354.

[37] X. Sauvage, Y. Ivanisenko, The role of carbon segregation on nanocrystallisation of pearlitic steels processed by severe plastic deformation, J. Mater. Sci. 42 (5) (2007) 1615–1621, http://dx.doi.org/10.1007/s10853-006-0750-z.

[38] J. Takahashi, Atom probe study on microstructure change in severely deformed pearlitic steels: Application to rail surfaces and drawn wires, IOP Conf. Ser. Mater. Sci. Eng. 219 (2017) 012007, http://dx.doi.org/10.1088/1757-899X/219/1/012007.

[39] J. Ahlström, B. Karlsson, Modelling of heat conduction and phase transformations during sliding of railway wheels, Wear 253 (1–2) (2002) 291–300, http://dx.doi.org/10.1016/S0043-1648(02)00119-9.

[40] J. Ahlström, Residual stresses generated by repeated local heating events – Modelling of possible mechanisms for crack initiation, Wear 366–367 (2016) 180–187, http://dx.doi.org/10.1016/j.wear.2016.05.029.

[41] Q. Lian, H. Zhu, G. Deng, X. Wang, H. Li, X. Wang, Z. Liu, Evolution of thermally induced white etching layer at rail surface during multiple wheel/train passages, Int. J. Fatigue 159 (2022) 106799, http://dx.doi.org/10.1016/j.ijfatigue.2022.106799.

[42] G. Antoni, T. Désoyer, F. Lebon, A combined thermo-mechanical model for Tribological Surface Transformations, Mech. Mater. 49 (2012) 92–99, http://dx.doi.org/10.1016/j.mechmat.2011.12.005.

[43] L. Thiercelin, L. Saint-Aimé, F. Lebon, A. Saulot, Thermomechanical modelling of the tribological surface transformations in the railroad network (white eching layer), Mech. Mater. (2020) 103636, http://dx.doi.org/10.1016/j.mechmat.2020.103636.

[44] British Steel, Rail steel grades - Steel compositions and properties, 2017, https://Britishsteel.Co.Uk https://britishsteel.co.uk/media/40810/steel-grade-dimensions-and-properties.pdf.

[45] O. Vargolici, P. Merino, A. Saulot, J. Cavoret, S. Simon, F. Ville, Y. Berthier, Influence of the initial surface state of bodies in contact on the formation of white etching layers under dry sliding conditions, Wear 366–367 (2016) 209–216, http://dx.doi.org/10.1016/j.wear.2016.06.023.

[46] R. Carroll, J. Beynon, Rolling contact fatigue of white etching layer: Part 1, Wear 262 (9–10) (2007) 1253–1266, http://dx.doi.org/10.1016/j.wear.2007.01.003.

[47] Y. Zhou, J. Peng, Z. Luo, B. Cao, X. Jin, M. Zhu, Phase and microstructural evolution in white etching layer of a pearlitic steel during rolling–sliding friction, Wear 362–363 (2016) 8–17, http://dx.doi.org/10.1016/j.wear.2016.05.007.

[48] C. Bernsteiner, G. Müller, A. Meierhofer, K. Six, D. Künstner, P. Dietmaier, Development of white etching layers on rails: Simulations and experiments, Wear 366–367 (2016) 116–122, http://dx.doi.org/10.1016/j.wear.2016.03.028.

[49] S. Simon, De la dynamique ferroviaire à l'accommodation microstructurale du rail - Contribution des TTS à la réponse tribologique des aciers - Cas du défaut de squat (Ph.D. thesis), INSA Lyon, 2014.

[50] B. Beausir, J.-J. Fundenberger, Analysis Tools for Electron and X-ray diffraction, ATEX - software, 2017, www.atex-software.eu.

[51] A. Al-Juboori, H. Zhu, D. Wexler, H. Li, C. Lu, A. McCusker, J. McLeod, S. Pannila, J. Barnes, Characterisation of White Etching Layers formed on rails subjected to different traffic conditions, Wear 436–437 (2019) 202998, http://dx.doi.org/10.1016/j.wear.2019.202998.

[52] J. Takahashi, K. Kawakami, M. Ueda, Atom probe tomography analysis of the white etching layer in a rail track surface, Acta Mater. 58 (10) (2010) 3602–3612, http://dx.doi.org/10.1016/j.actamat.2010.02.030.

[53] V. Gavriljuk, Decomposition of cementite in pearlitic steel due to plastic deformation, Mater. Sci. Eng. A 345 (1–2) (2003) 81–89, http://dx.doi.org/10.1016/S0921-5093(02)00358-1.

[54] A. Saulot, Analyse tribologique du contact roue-rail Modélisation et expérimentations – Cas de l'usure ondulatoire (Ph.D. thesis), INSA Lyon, 2005.

[55] W.J. Nam, C.M. Bae, Void initiation and microstructural changes during wire drawing of pearlitic steels, Mater. Sci. Eng. A 203 (1–2) (1995) 278–285, http://dx.doi.org/10.1016/0921-5093(95)09826-7.

[56] X. Zhang, A. Godfrey, N. Hansen, X. Huang, W. Liu, Q. Liu, Evolution of cementite morphology in pearlitic steel wire during wet wire drawing, Mater. Charact. 61 (1) (2010) 65–72, http://dx.doi.org/10.1016/j.matchar.2009.10.007.

[57] A.J. Perez-Unzueta, J.H. Beynon, Microstructure and wear resistance of pearlitic rail steels, Wear 162–164 (1993) 173–182, http://dx.doi.org/10.1016/0043-1648(93)90498-B.

[58] R. Pan, R. Ren, C. Chen, X. Zhao, Formation of nanocrystalline structure in pearlitic steels by dry sliding wear, Mater. Charact. 132 (2017) 397–404, http://dx.doi.org/10.1016/j.matchar.2017.05.031.

[59] W. Lojkowski, Y. Millman, S. Chugunova, I. Goncharova, M. Djahanbakhsh, G. Bürkle, H.-J. Fecht, The mechanical properties of the nanocrystalline layer on the surface of railway tracks, Mater. Sci. Eng. A 303 (1–2) (2001) 209–215, http://dx.doi.org/10.1016/S0921-5093(00)01948-1.

[60] F. Bucher, T. Klimpel, K. Johnson, Two-dimensional normal and tangential rail/wheel contact with rough surfaces, in: Tribology Series, vol. 39, Elsevier, 2001, pp. 551–562, http://dx.doi.org/10.1016/S0167-8922(01)80138-3.

[61] Y. Berthier, S. Descartes, M. Busquet, E. Niccolini, C. Desrayaud, L. Baillet, M.C. Baietto-Dubourg, The role and effects of the third body in the wheel-rail interaction, Fatigue Fract. Eng. Mater. Struct. 27 (5) (2004) 423–436, http://dx.doi.org/10.1111/j.1460-2695.2004.00764.x.

[62] F.W. Carter, On the action of a locomotive driving wheel, Proc. R. Soc. Lond. Ser. A 112 (760) (1926) 151–157, http://dx.doi.org/10.1098/rspa.1926.0100.

[63] K.L. Johnson, Contact Mechanics, Cambridge University Press, Cambridge [Cambridgeshire] ; New York, 1985.

[64] J.J. Kalker, in: G.M.L. Gladwell (Ed.), Three-Dimensional Elastic Bodies in Rolling Contact, in: Solid Mechanics and Its Applications, vol. 2, Springer Netherlands, Dordrecht, 1990, http://dx.doi.org/10.1007/978-94-015-7889-9.

[65] J.J. Kalker, Modification of the Two-Body Contact Conditions to Account for the third Body, in: D. Dowson, C.M. Taylor, T.H.C. Childs, M. Godet, G. Dalmaz (Eds.), Tribology Series, in: Wear Particles: Frorn the Cradle to the Grave, vol. 21, Elsevier, 1992, pp. 183–189, http://dx.doi.org/10.1016/S0167-8922(08)70523-6.

[66] J.J. Kalker, D.F. Cannon, O. Orringer (Eds.), Rail Quality and Maintenance for Modern Railway Operation: International Conference on Rail Quality and Maintenance for Modern Railway Operation Delft June 1992, Springer Netherlands, Dordrecht, 1993, http://dx.doi.org/10.1007/978-94-015-8151-6.

[67] K. Knothe, S. Liebelt, Determination of temperatures for sliding contact with applications for wheel-rail systems, Wear 189 (1–2) (1995) 91–99, http://dx.doi.org/10.1016/0043-1648(95)06666-7.

[68] V. Linck, A. Saulot, L. Baillet, Consequence of contact local kinematics of sliding bodies on the surface temperatures generated, Tribol. Int. 39 (12) (2006) 1664–1673, http://dx.doi.org/10.1016/j.triboint.2006.04.005.

[69] M. Naeimi, S. Li, Z. Li, J. Wu, R.H. Petrov, J. Sietsma, R. Dollevoet, Thermomechanical analysis of the wheel-rail contact using a coupled modelling procedure, Tribol. Int. 117 (2018) 250–260, http://dx.doi.org/10.1016/j.triboint.2017.09.010.

[70] Q. Lian, G. Deng, A.K. Tieu, H. Li, Z. Liu, X. Wang, H. Zhu, Thermo-mechanical coupled finite element analysis of rolling contact fatigue and wear properties of a rail steel under different slip ratios, Tribol. Int. 141 (2020) 105943, http://dx.doi.org/10.1016/j.triboint.2019.105943.

[71] P. Zwierczyk, K. Váradi, Thermal Stress Analysis of a Railway Wheel in Sliding-Rolling Motion, J. Tribol. 136 (3) (2014) 031401, http://dx.doi.org/10.1115/1.4027544.

[72] J. Ivanisenko, W. Łojkowski, R.Z. Valiev, H.J. Fecht, The Strain Induced Cementite Dissolution in Carbon Steel - Experimental Facts and Theoretical Approach, Solid State Phenomena 94 (2003) 45–50, http://dx.doi.org/10.4028/www.scientific.net/SSP.94.45.

[73] P.W. Bridgman, Effects of High Shearing Stress Combined with High Hydrostatic Pressure, Phys. Rev. 48 (10) (1935) 825–847, http://dx.doi.org/10.1103/PhysRev.48.825.

[74] P.W. Bridgman, The Effect of Pressure on the Tensile Properties of Several Metals and Other Materials, J. Appl. Phys. 24 (5) (1953) 560–570, http://dx.doi.org/10.1063/1.1721329.

[75] M. Yajima, M. Ishii, M. Kobayashi, The effects of hydrostatic pressure on the ductility of metals and alloys, Int. J. Fract. Mech. 6 (2) (1970) http://dx.doi.org/10.1007/BF00189821.

[76] J. Lewandowski, P. Lowhaphandu, Effects of hydrostatic pressure on mechanical behaviour and deformation processing of materials, Int. Mater. Rev. 43 (4) (1998) 145–187, http://dx.doi.org/10.1179/imr.1998.43.4.145.